CrystEngComm

Accepted Manuscript

ROYAL SOCIETY OF CHEMISTRY

www.rsc.org/crystengcomm

An intermediate phase $(NH_4)_2V_4O_9$ and its effects on the hydrothermal synthesis of VO_2 (M) nanoparticles

Bingrong Dong,[1,] Nan Shen,[1] Chuanxiang Cao,[1] Zhang Chen,[2] Hongjie Luo,[1,2] Yanfeng Gao,[1,2]*

1 State Key Laboratory of High Performance Ceramics and Superfine Microstructure, Shanghai institute of Ceramics, Chinese Academy of Sciences, 1295 Dingxi, Shanghai 200050, China

2 School of Materials Science and Engineering, Shanghai University, 99 Shangda, Shanghai 200444, China

* Author for correspondence. Email: yfgao@shu.edu.ac.cn

Tel/Fax: +86-21-6990-6218

Abstract

The hydrothermal synthesis of VO_2 (M) nanoparticles is commonly considered as a result of the transformation of intermediate phase VO_2 (A) or VO_2 (B). Here we found a new intermediate phase $(NH_4)_2V_4O_9$ that appeared in the hydrothermal synthesis and played a crucial role in the formation of VO_2 (M) nanoparticles. Then mechanism for the transformation of intermediate $(NH_4)_2V_4O_9$ to VO_2 (M) was described as self-assembly—decomposition—nucleation—growth. Crystalline pure VO_2 nanoparticles were ultimately obtained and showed excellent thermochromic properties. The phase-transition temperature Tc of VO_2 (M) nanoparticles is approximate 65°C. Furthermore, VO_2 flexible foils on PET at a VO_2 solid content of 1.5-2.0% show excellent optical properties with luminous transmittance (T_{lum}) > 50% and solar energy modulation ability (ΔT_{sol}) > 15%.

Keywords: vanadium dioxide; intermediate; $(NH_4)_2V_4O_9$; thermochromism; phase-transition property

1 Introduction

Monoclinic/rutile vanadium dioxide VO_2 (M/R) undergoes a first-order reversible metal–insulator transition (MIT) at a critical temperature of 68 °C (341 K).[1] This thermally driven phase transition consists with a crystallographic transition from a high-temperature tetragonal rutile structure VO_2 (R, $P4_2/mnm$) to a low-temperature monoclinic VO_2 (M, $P2_1/c$), corresponding to V^{4+} along the rutile c-axis forming homo-polar bonds and undergoing a structural twist.[2] Meanwhile, the MIT is accompanied with remarkable changes in near-infrared optical properties. Thus VO_2 (M/R) is regarded as an attractive thermochromic material for energy-saving applications as smart windows.[3-5]

Among more than ten kinds of VO_2 metastable polymorphs, such as VO_2 (A)[6], VO_2 (B)[7], VO_2 (C)[8] and VO_2 (D)[9], only the M/R phase possesses the MIT character. However, it is difficult to prepare pure VO_2 (M/R) due to multivalence (from V^{3+} to V^{5+}), structural diversity and disordered defect structures of VO_2. Several methods have been reported to prepare VO_2 (M/R) particles, including hydrothermal synthsis[10, 11], thermolysis[12-14] or thermal reduction[15]. Among these methods, the hydrothermal method is more suitable for synthesizing nano-particles, while the thermolysis or thermal reduction methods is usually very hard to produce a pure phase VO_2 (M/R) in one step and leads to the formation of agglomerative nano-particles and uncontrollable morphology with a large amount of defects.

On the other hand, the hydrothermal method is advantageous to forming dispersed nano-particles. In 2008, Cao et. al[10] reported a prior success in the hydrothermal synthesis of pure single-crystal VO_2 nanoparticles in 2008 by mingling V_2O_5 and oxalic acid ($H_2C_2O_4$) at 240 °C. Since then, some studies have been carried out to explore the synthesis mechanism of VO_2 (M/R) in the V_2O_5 - $H_2C_2O_4$ system and it is usually considered that the formation of VO_2 (M/R) was obtained by transformation of some metastable phases, such as VO_2 (A) and VO_2 (B)[16, 17]. Further, other reaction systems have been continuously proposed. Wu et. al[18] used $V(OH)_2NH_2$ as precursor to synthesize VO_2 (M) at 200 °C, and found that the acid condition was essential for

to avoid the fast aggregation of detached MO_6 octahedra or their small clusters. Gao et. al[19] synthesized pure-phase VO_2 (M/R) particles using a V_2O_5-N_2H_4·HCl system, and had controlled sizes and restricted the aggregation of VO_2 nanoparticles by doping Sb^{3+}. Chen et. al[20] developed a "heating-up" process that induced burst-nucleation by decomposition of precursor $VO(OH)_2$.

In this work, the growth of VO_2 nanoparticles was realized by decomposition of a new intermediate phase $(NH_4)_2V_4O_9$ during the hydrothermal reaction in a V_2O_5-N_2H_4·HCl-NH_3·H_2O system. To the best of our knowledge, there was scarcely any information of the ammonium vanadate $(NH_4)_2V_4O_9$ and its transformation into VO_2. During our low-temperature hydrothermal experiment, a well-crystallized, square-bulk/sheet $(NH_4)_2V_4O_9$ was obtained, which was transformed to VO_2 (M) nanoparticles. Based on this result, a "two-step" hydrothermal method was designed to study the evolution from intermediate $(NH_4)_2V_4O_9$ to VO_2 (M) by setting two reaction periods (first reacting at 230°C, then heating up to 300°C) and pure fine crystalline VO_2 nanoparticles were ultimately obtained. This finding shows significant referential value on VO_2 (M/R) nanoparticles synthesis.

Simultaneously, the VO_2 (M) nanoparticles prepared by this "two-step" hydrothermal method showed excellent thermochromic optical properties. These VO_2 (M) nanoparticles had a high latent heat during MIT (ΔH = 31.15 J/g), indicating that the VO_2 (M) nanoparticles were highly crystalline. A VO_2-PET composite film by casting these VO_2 (M) nanoparticles displayed excellent optical-switching characters (T_{lum} = 50.3%, ΔT_{sol} = 17.5%, at VO_2 solid content 2.0%).

2 Experimental Methods

All reagents were purchased from the Sinopharm Chemical Reagent Co., Ltd., and used without further purification. Vanadium pentoxide (V_2O_5, analytically pure) and diamide hydrochloride (N_2H_4·HCl, analytically pure) were employed as starting materials to prepare a VO^{2+} solution. Concentrated HCl (6 mL, 38%) and a solution containing 1 g of N_2H_4·HCl were added into an aqueous suspension (20 mL) containing 3.5 g of V_2O_5. The solution was treated with a small amount of V_2O_5 or

$N_2H_4 \cdot HCl$ until it contained no VO^{2+} or V^{3+} and was then filtered to form a clear VO^{2+} solution (pH $\approx$ 1). Then an amount of ammonia was added into the solution until the pH $\approx$ 8. The solution was stirred for 10 min and then transferred to a 50 mL stainless steel autoclave. The hydrothermal reaction was carried out at different temperatures for defined time. The final black product was separated by centrifugation and washed with water and ethanol.

Characterization.

The morphologies and element distributions of the resulting powders were analysed via transmission electron microscopy (TEM, JEM2010, JEOL, Japan) and scanning electron microscopy (SEM, Magellan 400), respectively. The crystalline phases of the nanoparticles were determined by X-ray diffraction (XRD, Model D/Max 2550 V, Rigaku, Japan). The phase transition temperatures of the products were measured via differential scanning calorimetry (DSC, DSC200F3, NETZSCH) in nitrogen flow in the temperature range from 0 °C to 100 °C at a heating rate of 10 °C min^{-1}. The decomposition process of the intermediate phase was investigated by thermos-gravimetry/differential thermal analysis (TG-DTA, STA 449C, Netzsch, Selb, Germany) at a heating rate of 10 °C min^{-1}. Fourier transform infrared spectroscopy (FTIR, Nicolet, Magna 560) was used to detect the chemical bonding of samples. The thermochromic properties were evaluated by the VO_2-PET composite films. For measurements, the VO_2 powders were uniformly dispersed in polyurethane after surface modification by poly(vinylpyrrolidone) (PVP), and then deposited on polyethylene terephthalate (PET) via knife-coating, and finally dried at 70 °C. The optical transmittance characteristics were monitored using a Hitachi U-4100 UV-visible-near-IR spectrophotometer equipped with a film heating unit in the wavelength range of 350-2600 nm. The temperature was measured using a thermocouple in contact with the films, which was controlled through a temperature-control unit.

3 Results and discussion

3. 1 The synthesis of intermediate $(NH_4)_2V_4O_9$

A new, well-crystallized ammonium vanadate $(NH_4)_2V_4O_9$ was prepared as an intermediate. The synthesis of VO_2 (M) (JCPDS No.:72-0514) was a result of transformation from this intermediate at increased temperatures. The XRD patterns (Fig. 1a) of the samples obtained at reacting temperature 230 or 240 °C suggest the formation of $(NH_4)_2V_4O_9$ (JCPDS No.: 23-0791); at 210 or 220°C, peaks for $(NH_4)_2V_4O_9$ and some unknown peaks were detected. The unknown phase is most likely vanadium oxide hydrate $(VO_2)_x \cdot yH_2O$. At 250 or 260°C, $(NH_4)_2V_4O_9$ peaks were notably weakened and VO_2 (M) peaks appear. It is obvious that the 10° peak of $(NH_4)_2V_4O_9$ gradually strengthens from 210 to 240°C, which is accompanied by the disappearance of peaks of the unknown $(VO_2)_x \cdot yH_2O$ hydrate phase; while the 10° peak gradually weakens from 240 to 260 °C, as a replacement, peaks for VO_2(M) appear. It reveals that $(NH_4)_2V_4O_9$ is synthesized by the decomposition of $(VO_2)_x \cdot yH_2O$, and $(NH_4)_2V_4O_9$ into VO_2 (M). Thus $(NH_4)_2V_4O_9$ plays a crucial role in VO_2 growth and is necessary to study.

The XRD patterns (Fig. 1b) show the reaction process of $(NH_4)_2V_4O_9$ at 230 °C for different times. With the reaction time increasing, the obtained products changed from non-crystalline powders to coexistence of $(NH_4)_2V_4O_9$ and $(VO_2)_x \cdot yH_2O$ hydrate and ultimately transformed into well-crystallized $(NH_4)_2V_4O_9$. Meanwhile, with the 10° peak of $(NH_4)_2V_4O_9$ gradually strengthening, the crystallinity of $(NH_4)_2V_4O_9$ becomes better, which is accompanied with morphology change.

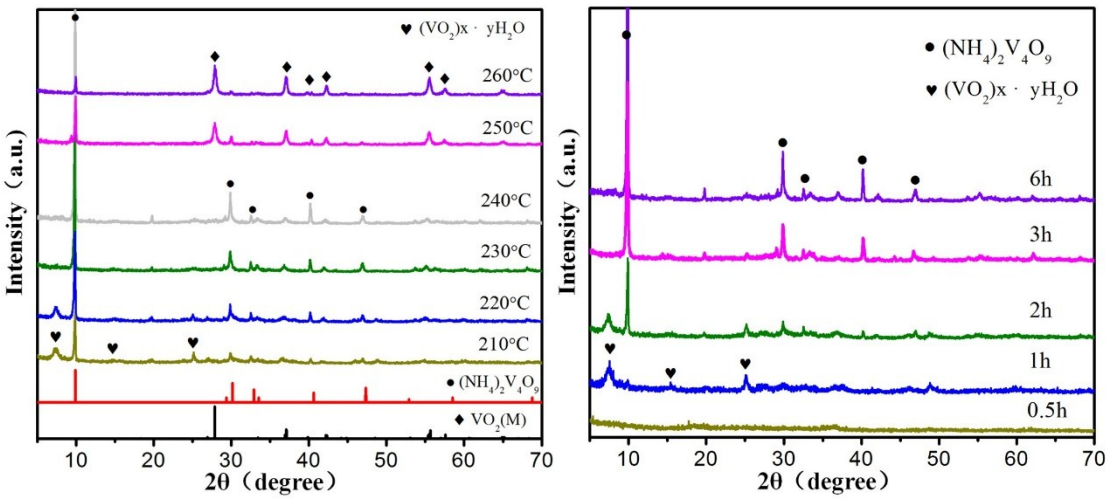

Fig. 1 XRD patterns of samples obtained (a) at different temperatures for 6 h; red pattern refers to $(NH_4)_2V_4O_9$ (JCPDS No.: 23-0791) and black pattern refers to VO_2 (M) (JCPDS No.:72-0514); (b) at 230 °C for different time;

The FTIR spectrum of the obtained $(NH_4)_2V_4O_9$ is shown in Fig. 2a. There are several absorption bands at 3250, 1644, 1434, 1403, 1020, 953,800, 578 and 493 cm^{-1}, respectively, which can be assigned to the different excitations of V-O structure. The bands at 1020 and 953 cm^{-1} are due to V=O stretching of distorted octahedra and distorted square pyramids, while the bands at 800 cm^{-1} are assigned to asymmetric stretching vibration of V–O–V bonds.[21] The absorption band at 578 and 493 cm^{-1} are due to stretching vibrations of the groups incorporating a bridging oxygen coordinated to three or four vanadium atoms.[22] The other two broad absorption bands at about 1420 and 3250 cm^{-1} are attributed to the symmetric bending vibration and the asymmetric stretching vibrations of NH^{4+}.[23] In addition, H-O-H bending motion is identified by the characteristic band at 1644 cm^{-1}.[24] To further determine whether the water is the crystallization water or physically adsorbed water, TG/DTA test was carried out. The results are shown in Fig. 2b. Clearly, there is a broad peak around 100 °C, with a weight loss of about 1.3%, which is attributed to the evaporation of adsorbed water. And there is another strong exothermal peak at 364 °C, similar to the decomposition temperature of $NH_4V_3O_8$[25]， and the weight loss is about 5.1% due to the decomposition of ammonium salt according to the equation:

$$(NH_4)_2V_4O_9 + O_2 \rightarrow V_2O_5 + 2NH_3\uparrow + H_2O\uparrow \qquad \Delta m = -5.2\%$$

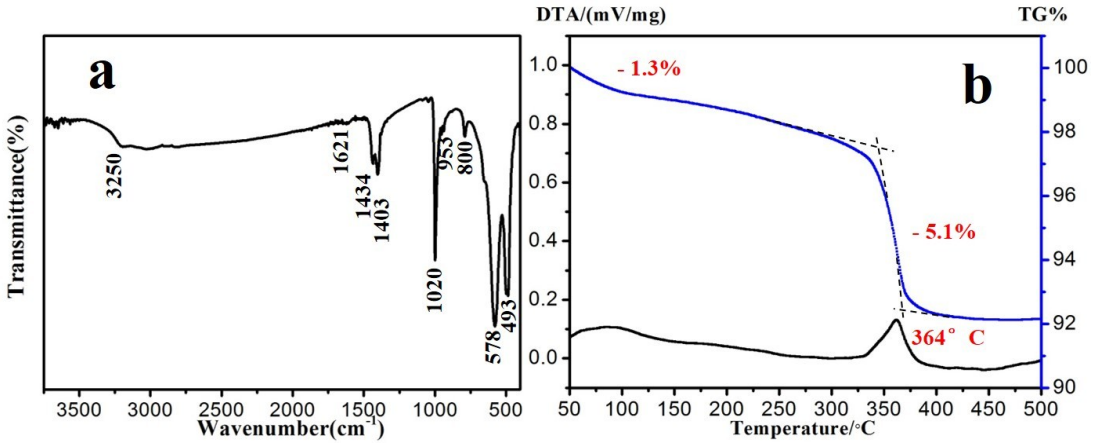

Fig. 2 (a) FTIR spectrum and（b）TG-DTA curve of $(NH_4)_2V_4O_9$ prepared at 230 °C for 6 h；

Fig. 3 shows the morphology evolution from vanadium oxide hydrate $(VO_2)_x \cdot yH_2O$ to intermediate phase $(NH_4)_2V_4O_9$ at 230 °C for different times. As can be seen, the morphology of $(VO_2)_x \cdot yH_2O$ (prepared at 230 °C for 1 h) is thin nano-belts with 100-400 nm in width and 200-2000 nm in length (Fig. 3a). When the reaction time is prolonged to 2 h, the nano-belts gradually weave and combine into a square sheet of 2.5 μm long (Fig. 3b-c). According to XRD patterns in Fig. 1b, the sample prepared at 230 °C for 2 h is the coexistence of $(NH_4)_2V_4O_9$ and $(VO_2)_x \cdot yH_2O$ hydrate. Those results suggest that $(VO_2)_x \cdot yH_2O$ nano-belts self-assemble into $(NH_4)_2V_4O_9$ square sheets. Consequently, well-crystallized $(NH_4)_2V_4O_9$ square sheets was obtained at 230 °C for 3 h with a rectangular cross-section (thickness 50 nm) shown in Fig. 3d. However, with continuing to prolong time to 6 h, ultra-square bulk $(NH_4)_2V_4O_9$ with length about 10 μm was obtained (Fig. 3e) and several stepped surfaces can be clearly observed in Fig. 3f (magnified region of a blue oval in Fig. 3e). It indicates that square sheets self-assemble stack by stack and grow into ultra-square bulks with the direct evidence of the size of $(NH_4)_2V_4O_9$ square sheet/bulk enlarging from 3 μm to 10 μm and the stepped surfaces. Thus during hydrothermal process, there are no other VO_2 metastable phases or VO_2 precursors and only square-sheet/bulk $(NH_4)_2V_4O_9$ is synthesized ultimately.

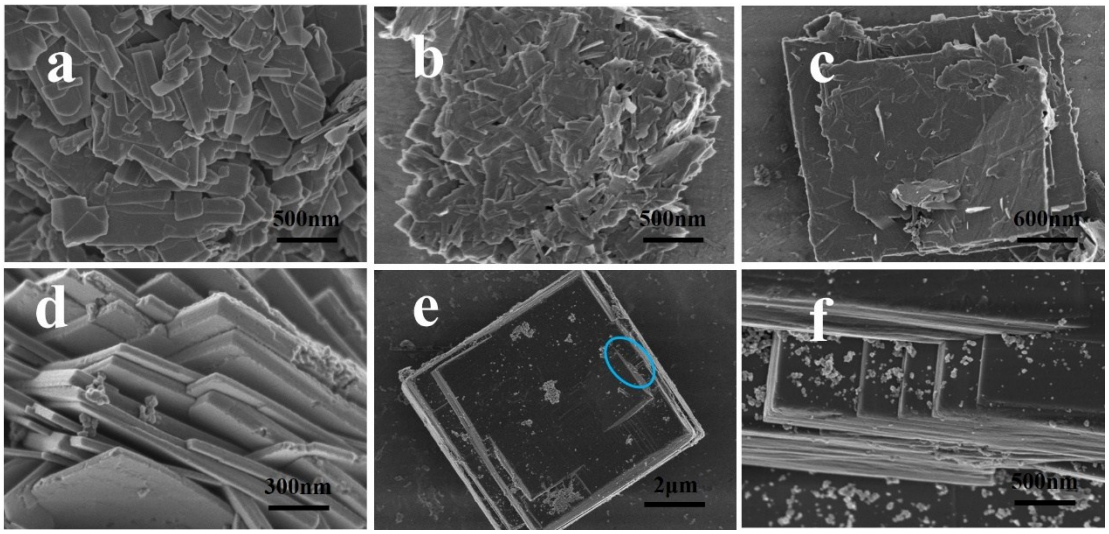

Fig. 3 SEM images of samples prepared at 230 °C for different time (a) 1 h; (b) 2 h; (c) 2 h; (d) 3

h; (e) 6 h; (f)6 h;

Fig. 4 shows TEM images of ultra-square $(NH_4)_2V_4O_9$ of 14 μm in length obtained at 230 °C for 6 h. The corresponding SAED and lattice-resolved HRTEM images in Fig. 4b indicate high crystallinity according to clear lattice fringes with an interplanar spacing of about 0.304 nm.

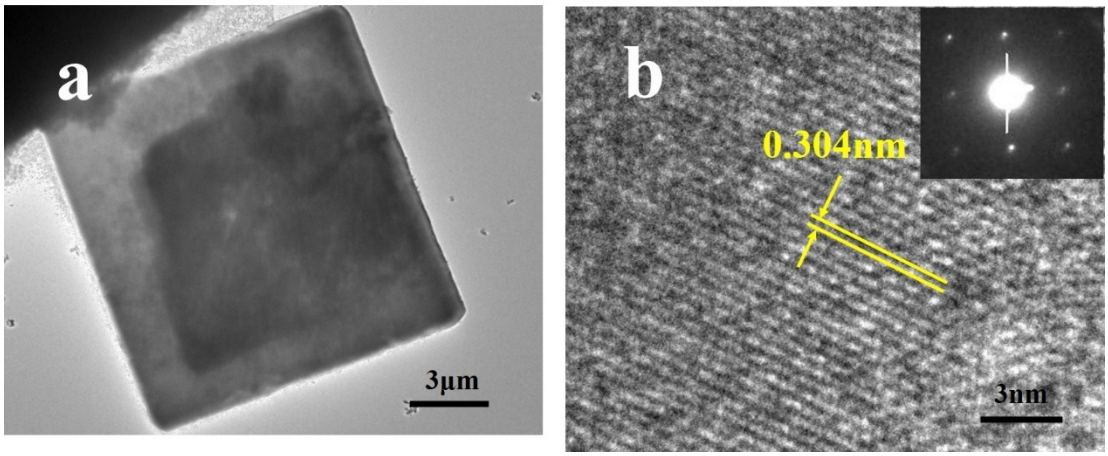

Fig. 4 (a) TEM images of the $(NH_4)_2V_4O_9$ square bulks obtained at 230 °C for 6 h; (b) lattice-resolved HRTEM image and SAED pattern acquired from the ultra-square bulks;

3. 2 A "two-step" hydrothermal method

Herein, to further evaluate the effect of the intermediate $(NH_4)_2V_4O_9$ on the preparation of VO_2 (M), a "two-step" hydrothermal process was designed to study the evolution from $(NH_4)_2V_4O_9$ to VO_2 (M) by setting two reaction periods. The concrete experimental procedure is as follow. First heating up to 230 °C and reacting for 3 h, which can produce intermediate $(NH_4)_2V_4O_9$ completely (XRD pattern shown in Fig. 5(gray). Then rapidly heating up to 260 - 300 °C and keeping 24 h to support VO_x to nucleate and grow. During the second period from 260 to 280 °C, peaks for VO_2 (M) began to emerge and gradually increased, while the 10° peak for $(NH_4)_2V_4O_9$ significantly weakened (Fig. 5). It suggests that the intermediate $(NH_4)_2V_4O_9$ gradually transforms to VO_2 (M) without other phases or precursors participating during the second hydrothermal reaction period. Finally, $(NH_4)_2V_4O_9$ totally disappears and form fine crystalline VO_2 (M) with the temperature increasing to

290-300 °C. It reveals a new synthesis mechanism of VO_2 (M) nanoparticles via the decomposition of intermediate phase $(NH_4)_2V_4O_9$ during a "two-step" hydrothermal process.

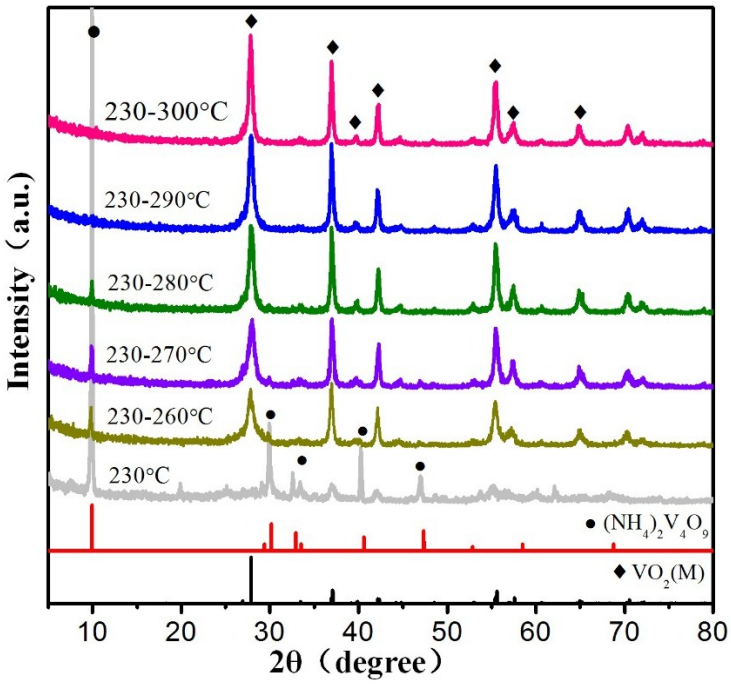

Fig. 5 XRD patterns of samples obtained by a "two-step" hydrothermal process; red pattern refers to $(NH_4)_2V_4O_9$ (JCPDS No.: 23-0791) and black pattern refers to VO_2 (M) (JCPDS No.:72-0514);

Fig. 6 shows the temperature-dependent evolution process from well-crystallized, square-sheet intermediate $(NH_4)_2V_4O_9$ to VO_2 (M) nanoparticles. The $(NH_4)_2V_4O_9$ square sheets with typical rectangular nanostructures of smooth edges were prepared during the first period at 230 °C for 6 h (Fig. 6a). However, after rapidly heating up to 260 °C and keeping at this temperature for 24 h, bud-like nanoparticles were observed to grow outwards from the smooth edges of square sheets and the roots of bud-like nanoparticles still perfectly connected with the edges, as shown in Fig. 6b. Then the edges of square sheets were consumed to generate VO_2 (M) nanoparticles in quantity as the temperature increased to 270 °C (Fig. 6c). With further reaction, the square sheets were gradually consumed from outside to inside (Fig. 6d), leading to large amounts of VO_2 (M) nanoparticles coexisting with incompletely reacted $(NH_4)_2V_4O_9$

sheets. Finally the VO_2 (M) nanoparticles with small particles (around 20 - 50 nm) and several short rods (length 100 - 200 nm) structure are obtained shown in Fig. 6e. The corresponding SAED image and lattice-resolved HRTEM image shown in Fig. 6f' corroborate the single crystalline nature of the nanostructures and the interplanar spacing is calculated to be around 0.312 nm, which is indexed to the (011) facet of VO_2 (M) and indicative of the (011) preferential growth direction.

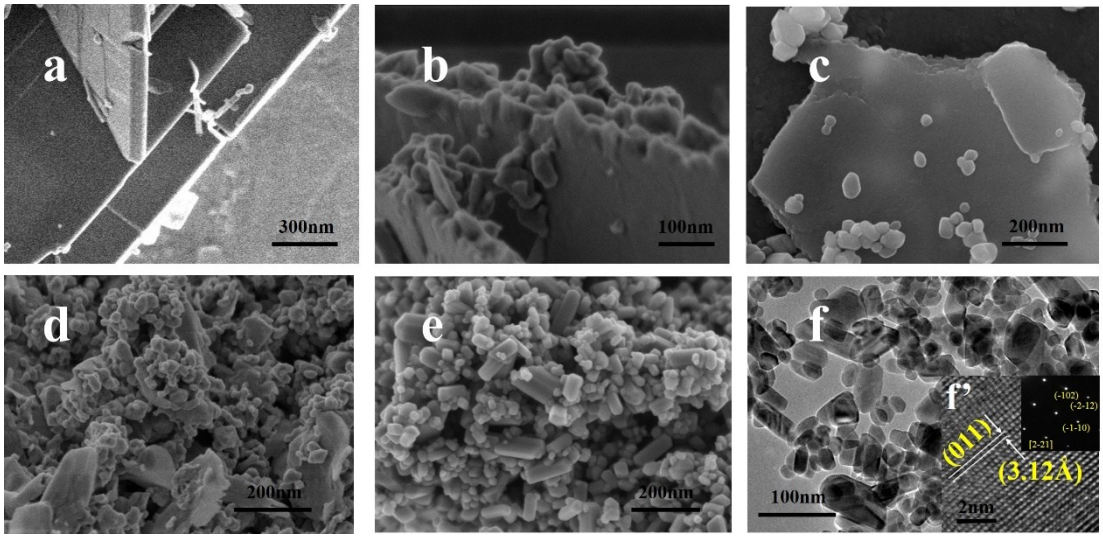

Fig. 6 SEM images of samples prepared via a "two-step" hydrothermal process (a) 230 °C; (b) 230 - 260 °C; (c) 230 – 270 °C; (d) 230 – 280 °C; (e) 230 – 300 °C; (f) TEM images of samples prepared at 230 – 300 °C; (f') lattice-resolved HRTEM image and SAED pattern acquired from particles in (f).

Here we present a schematic description of the mechanism for forming $(NH_4)_2V_4O_9$ ultra-square bulks and VO_2 (M) nanoparticles is presented in Fig. 7. It is well known that the condensation of monomers is due to the attraction of positively and negatively charged groups. The six-fold coordinated neutral monomers $[VO(OH)_2(OH_2)_3]$[26] appear in solution and the condensation of the vanadium monomers can occur either via an olation or an oxolation process as shown below[27]

Olation $\quad V\text{–}OH + V\text{–}OH_2 \rightarrow -V\text{–}OH\text{–}V- + H_2O \quad$ (fast)

Oxolation $\quad V\text{–}OH + HO\text{–}V- \rightarrow -V\text{–}O\text{–}V- + H_2O \quad$ (slow)

During the olation reaction, the corner-linked octahedrons form chains along the

H_2O–V–OH direction while edge-linked octahedrons connect along HO–V–OH direction in an oxolation process.[28] In the z direction (H_2O–V=O), there are no H_2O–V–OH groups present, which leads to the formation of a 1D/2D-vanadium oxide network within the xy plane.[25] Thus belt-like $(VO_2)_x \cdot yH_2O$ hydrate particles are generated in this case.

As for the morphology evolution of a crystal, the reaction proceeds toward lower systematic energy to maintain a stable system and provide driving forces for oriented attachment. Therefore the nano-belts attach and combine together spontaneously via electrostatic interaction and the hydrogen bonding of NH^{4+} to reduce surface energy.[29] Finally $(NH_4)_2V_4O_9$ square sheets are formed like a bamboo mat. During the second high-temperature hydrothermal reaction, $(NH_4)_2V_4O_9$ begins to decompose or dissolve, because the temperature is close to its intrinsic decomposition temperature (364 °C) revealed by DTA result in Fig. 2b. Thus the VO_x bud-like nuclei are generated from the consumption of the edges of $(NH_4)_2V_4O_9$. As a result, the edges gradually consume and finally grow into fine crystalline VO_2 (M) nanoparticles. In summary, the formation mechanism of VO_2 (M) nanoparticles can be described as a self-assembly—decomposition—nucleation—growth process.

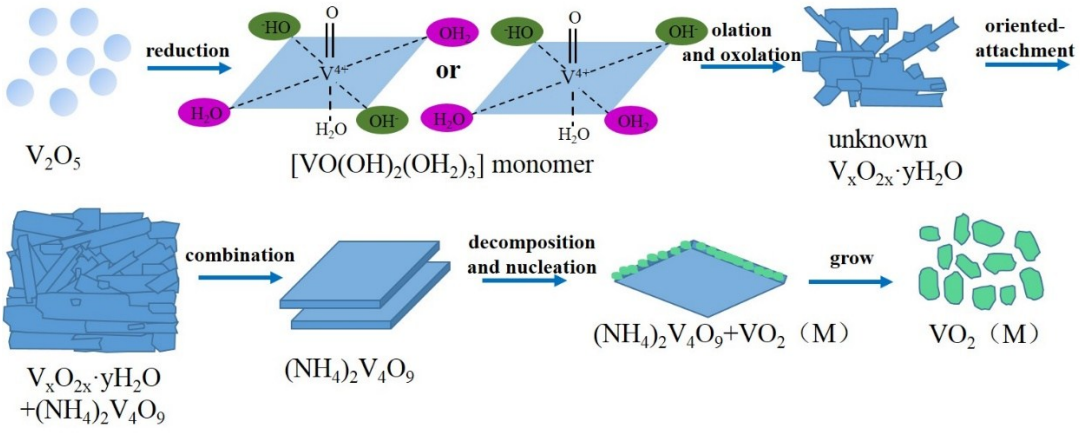

Fig. 7 A schematic illustration of the evolutions of $(NH_4)_2V_4O_9$ square bulks and VO_2 nanoparticles.

3. 3 The phase-transition and thermochromic properties

The metal–insulator transition (MIT) of VO_2 nanoparticles prepared by a "two-step" hydrothermal method is characterized via DSC as shown in Fig. 8. The VO_2 (M) nanoparticles possess an excellent MIT property, with the phase transition enthalpy ΔH = 31.15 J/g and phase transition temperature $Tc_{-300°C}$ = 65.9 °C, which is a bit lower than that of 68 °C for bulk VO_2. However, during the second stage (the temperature of 260 °C), the DSC endothermic peak appears two phase transition temperatures (Tc_1 = 58.0 °C and Tc_2 = 63.3°C respectively) lower than 65.9 °C. The decreased Tc of pure VO_2 nanoparticles is always ascribed to multiple factors, including defects[30-32], stress[33], size effects[34, 35] and non-stoichiometry[36]. Thus the Tc_1 and Tc_2 decrease is mainly because of the influence of poor crystallinity and defects.[37] Tc_1 is possibly corresponding to the bud-like VO_2 nucleus growing out from $(NH_4)_2V_4O_9$ square sheets, as shown in Fig. 6b; The Tc_2 corresponds to the irregular VO_2 nanoparticles that are just free from $(NH_4)_2V_4O_9$ square sheets but have not yet formed into the fine crystallinity VO_2 nanoparticles. Therefore $Tc_1 < Tc_2$ based on their crystallinity, and much lower than $Tc_{-300°C}$ = 65.9 °C. Moreover, at the second period temperature increasing from 270 to 290 °C, Tc gradually increases slightly from 62.5 °C to 63.8 °C and it is accordance with the explanation of the crystallinity change of VO_2 nanoparticles.

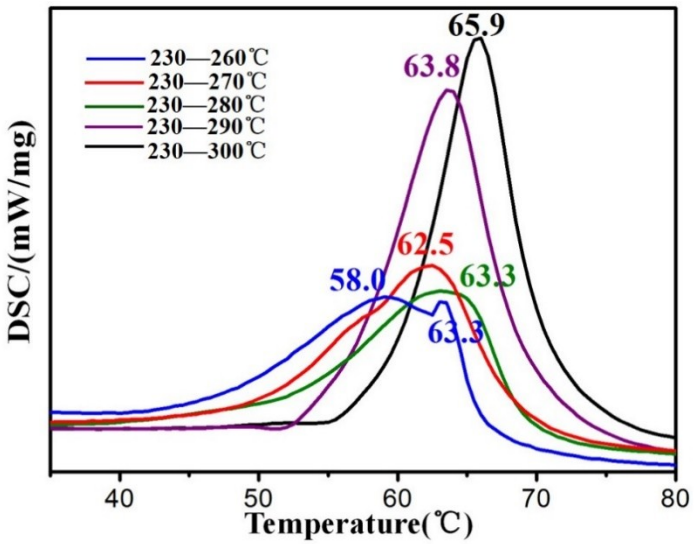

Fig. 8 DSC heat flow of the VO_2 nanoparticles samples prepared via a "two-step" hydrothermal process;

To further investigate the optical properties of VO_2 (M/R) nanoparticles obtained by the "two-step" hydrothermal method, VO_2-PET composite films were prepared by casting VO_2 dispersion on PET substrate with a fixed thickness but varied VO_2 solid contents. For all samples, the integral visible transmittance (T_{lum}, 350 - 750 nm) and solar transmittance (T_{sol}, 240 - 2600 nm) were obtained based on the measured spectra using the following equation:

$$T_i = \int \varphi_i(\lambda) T(\lambda) d\lambda / \int \varphi_i(\lambda) d\lambda \qquad (1)$$

$$\Delta T_{sol} = T_{sol}(T < T_c) - T_{sol}(T > T_c) \qquad (2)$$

where $T(\lambda)$ denotes the transmittance at wavelength λ, i denotes 'lum' or 'sol' for the calculations, T and ΔT_{sol} are the temperature and solar modulation ability, respectively; φ_{lum} is the standard luminous efficiency function for the photopic vision according to CIE 1931 standards, and φ_{sol} is the solar irradiance spectrum for the air mass 1.5 (corresponding to the sun standing 37° above the horizon) according to ASTM G173-03 Reference Spectra.

It is well known that most of the solar energy is distributed in the visible (350 - 750 nm) and near-infrared (750 - 1500 nm) regions. This fact indicates that the solar modulation ability of VO_2 films is dominated by the transmittance differences in this wavelength region across the phase transition. Interestingly, VO_2 films exhibit distinct transmittance differences before and after MIT in the near infrared (750 - 1500 nm) region than other wave regions shown in Fig. 9a (solid lines for 20°C and dash lines for 90°C). With increasing VO_2 solid content, the transmittance differences (750 - 1500 nm) are distinctly enlarged. Thus the transmittance difference at λ = 1300 nm (ΔT_{1300}) enhanced from 16.4% to 51.2%, with the VO_2 solid content increasing from 0.5% to 2.5%, as shown in Table. 1. It can be explained by surface plasmon resonance that occurs at temperatures (90 °C) higher than Tc.[38] Sufficient conduction electrons on the surface excited by light take part in resonant excitation and collective oscillations known as localized surface plasmon resonance (LSPR).[39] LSPR results in a strong absorption in the near-infrared (750 - 1500 nm) region and the phenomena is enhanced with increasing VO_2 solid contents. The solar modulation ability (ΔT_{sol})

reaches the maximum of 19.4% at a VO_2 solid content 2.5%.

Moreover, Fig. 9b and Table 1 clearly exhibit the relationship between the visible transmittance (T_{lum}) and solar modulation ability (ΔT_{sol}). T_{lum} reached 74.5% with ΔT_{sol} 5.6% at a VO_2 solid content 0.5%; while the ΔT_{sol} maximum 19.4% with T_{lum} 42.2% was obtained at a VO_2 solid content 2.5%. It indicates that it is conflicting on improving T_{lum} and ΔT_{sol}. Thus with the VO_2 solid content of 2.0%, T_{lum} 50.3% and ΔT_{sol} 17.5% reached a good balance. It also indicates the optimal VO_2 solid content is around 1.5~2.0% that meet the requirement of $T_{lum} > 50\%$ and $\Delta T_{sol} > 15\%$ from the curves in Fig. 9b. Furthermore, as shown in Table 2, the T_{lum} and ΔT_{sol} values in this work are superior or close to previously reported results, such as single-layered films (ΔT_{sol} is 6.7% at $T_{lum} = 41\%$[40]; ΔT_{sol} is only 7.1% at $T_{lum} = 50\%$[41]), porous films($\Delta T_{sol} = 14.1\%$ and $T_{lum} = 43\%$[42]) and multi-layered films (a TiO_2–VO_2–TiO_2–VO_2–TiO_2 five-layered film, $\Delta T_{sol} = 12.1\%$ and $T_{lum} = 45\%$[43]; a double-layered structure VO_2/TiO_2, $\Delta T_{sol} = 15.1\%$ and $T_{lum} = 49.5\%$[44]).

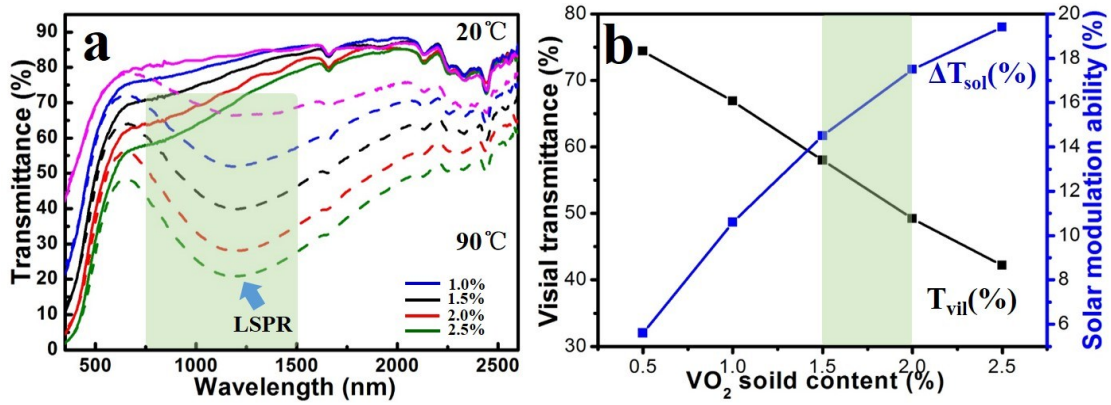

Fig. 9 (a) The transmittance spectra of VO_2-PET composite films at 20 and 90 °C with different solid content of VO_2; (b) The visible transmittance and solar modulation ability with different solid contents of VO_2.

Table 1 The solar energy control properties of VO_2-PET composite films with different VO_2 solid content.

VO_2 solid content	T_{lum}(%)		T_{sol}(%)		ΔT_{sol} (%)	ΔT_{1500}（%）
	20℃	90℃	20℃	90℃		
0.5%	74.4	74.0	76.6	71.0	5.6	16.4

1.0%	67.4	66.0	70.9	60.4	10.6	28.6
1.5%	59.0	56.4	65.0	50.0	15.0	37.4
2.0%	50.3	47.2	57.7	40.2	17.5	46.7
2.5%	42.8	40.0	52.1	32.6	19.4	51.2

Table 2 Comparison between this work and previously reported studies on T_{lum}, ΔT_{sol} of VO_2 films or foils

System	ΔT_{sol} (%)	ΔT_{lum} (%)
Singer-layered VO_2 film[40]	6.7	50
porous films[42]	14.1	43
TiO_2–VO_2–TiO_2–VO_2–TiO_2 five-layered film[43]	12.1	45
double-layered structure VO_2/TiO_2 film[44]	17.5	46.7
this work (at VO_2 soild content 2%)	17.3	50.3

4 Conclusions

In this work, a new intermediate $(NH_4)_2V_4O_9$ square sheet/bulk was discovered during a mild hydrothermal process using a V_2O_5-$N_2H_4 \cdot HCl$-$NH_3 \cdot H_2O$ system; then through designing a "two-step" hydrothermal method by setting two reaction periods (first reacting at 230 °C, then heating up to 300 °C), a new mechanism for the transformation of intermediate $(NH_4)_2V_4O_9$ square sheets to VO_2 (M) nanoparticles was proposed as self-assembly—decomposition—nucleation—growth. Those findings show significant referential value on VO_2 (M/R) nanoparticles synthesis. The as-obtained pure VO_2 (M) showed excellent thermochromic optical properties. The phase-transition temperature was 58.0 °C to 65.9 °C for different crystallinity.

Moreover at a VO_2 solid content of 2%, the VO_2-PET film exhibited relatively high visible transmittances T_{lum} = 50.3% and solar modulation ability ΔT_{sol} = 17.5%.

Acknowledgements

This study was supported in part by funds from MOST (2014AA032802), NSFC (State Outstanding Young Scholars, 51325203) and Shanghai Municipal Science and Technology Commission (15XD1501700).

References

1. F. J. Morin, *Phys. Rev. Lett*, 1959, **3**, 34-36.
2. J. Booth and P. Casey, *Phys. Rev. Lett.*, 2009, **103**, 086402.
3. Y. F. Gao, H. J. Luo, Z. T. Zhang, L. T. Kang, Z. Chen, J. Du, M. Kanehira and C. X. Cao, *Nano Energy*, 2012, **1**, 221-246.
4. Y. F. Gao, S. B. Wang, H. J. Luo, L. Dai, C. X. Cao, Y. L. Liu, Z. Chen and M. Kanehira, *Energy Environ. Sci.*, 2012, **5**, 6104.
5. T. D. Manning, I. P. Parkin, M. E. Pemble, D. Sheel and D. Vernardou, *Chem. Mater.*, 2004, **16**, 744-749.
6. J. Galy, *J. Solid State Chem.*, 1999, **148**, 224-228.
7. S. D. Zhang, B. Shang, J. L. Yang, W. S. Yan, S. Q. Wei and Y. Xie, *Phys. Chem. Chem. Phys.*, 2011, **13**, 15873–15881.
8. D. Hagrman, J. Zubieta, C. J. Warren, L. M. Meyer, M. M. J. Treacy and R. C. Haushalter, *J. Solid State Chem.*, 1998, **138**, 178-182.
9. L. Liu, F. Cao, T. Yao, Y. Xu, M. Zhou, B. Y. Qu, B. C. Pan, C. Z. Wu, S. Q. Wei and Y. Xie, *New J. Chem.*, 2012, **36**, 619.
10. C. X. Cao, Y. F. Gao and H. J. Luo, *J. Phys. Chem. C*, 2008, **112**, 18810-18814.
11. C. X. Cao, Y. F. Gao, L. T. Kang and H. J. Luo, *CrystEngComm*, 2010, **12**, 4048-4051.
12. X. D. Xiao, H. Zhang, G. Q. Chai, Y. M. Sun, T. Yang, H. L. Cheng, L. H. Chen, L. Miao and G. Xu, *Mater. Res. Bull.*, 2014, **51**, 6-12.
13. C. M. Zheng, J. L. Zhang, G. B. Luo, J. Q. Ye and M. M. Wu, *J. Mater. Sci.*, 2000, **35**, 3425-3429.
14. J. Q. Shi, S. X. Zhou, B. You and L. M. Wu, *Sol. Energy Mater. Sol. Cells*, 2007, **91**, 1856-1862.
15. J. Tian, F. Liu, C. M. Shen, H. R. Zhang, T. Z. Yang, L. H. Bao, X. J. Wang, D. T. Liu, H. Li, X. J. Huang, J. Q. Li, L. Q. Chen and H. J. Gao, *J. Mater. Res.*, 2007, **22**, 1921-1926.
16. S. D. Ji, Y. G. Zhao, F. Zhang and P. Jin, *J. Cryst. Growth*, 2010, **312**, 282-286.
17. S. D. Ji, F. Zhang and P. Jin, *Res. Chem. Intermed.*, 2011, **37**, 493-502.
18. C. Z. Wu, X. D. Zhang, J. Dai, J. L. Yang, Z. Y. Wu, S. Q. Wei and Y. Xie, *J. Mater. Chem.*, 2011, **21**, 4509-4517.
19. Y. F. Gao, C. X. Cao, L. Dai, H. J. Luo, M. Kanehira, Y. Ding and Z. L. Wang, *Energy Environ. Sci*, 2012, **5**, 8708.
20. Z. Chen, Y. F. Gao, L. T. Kang, C. X. Cao, S. Chen and H. J. Luo, *J. Mater. Chem. A*, 2014, **2**, 2718.

21. B. Azambre, M. J. Hudson and O. Heintz, *J. Mater. Chem.*, 2003, **13**, 385-393.
22. A. P. Jin, W. Chen, Q. Y. Zhu, Y. Yang, V. L. Volkov and G. S. Zakharova, *Thin Solid Films*, 2009, **517**, 2023-2028.
23. A. Dobley, K. Ngala, S. F. Yang, P. Y. Zavalij and M. S. Whittingham, *Chem. Mater.*, 2001, **13**, 4382-4386.
24. G. S. Zakharova, V. L. Volkov, C. Täschner, I. Hellmann, R. Klingeler, A. Leonhardt and B. Büchner, *Mater. Lett.*, 2011, **65**, 579-582.
25. G. S. Zakharova, C. Täschner, T. Kolb, C. Jahne, A. Leonhardt, B. Büchner and R. Klingeler, *Dalton Trans.*, 2013, **42**, 4897-4902.
26. Y. J. Zhou, S. D. Ji, Y. M. Li, Y. F. Gao, H. J. Luo and P. Jin, *J. Mater. Chem. C*, 2014, **2**, 3812.
27. J. Livage, *Coord. Chem. Rev.*, 1998, **178**, 999-1018.
28. G. S. Zakharova, V. L. Volkov, C. Täschner, I. Hellmann, A. Leonhardt, R. Klingeler and B. Büchner, *Solid State Commun.*, 2009, **149**, 814-817.
29. H. A. Abbood, H. Peng, X. H. Gao, B. E. Tan and K. X. Huang, *Chem. Eng. J.*, 2012, **209**, 245-254.
30. C. Z. Wu, F. Feng, J. Feng, J. Dai, J. L. Yang and Y. Xie, *J. Phys. Chem. C*, 2011, **115**, 791-799.
31. F. Guinneton, L. Sauques, J. C. Valmalette, F. Cros and J. R. Gavarri, *J. Phys. Chem. Solids*, 2005, **66**, 63-73.
32. K. Appavoo, D. Y. Lei, Y. Sonnefraud, B. Wang, S. T. Pantelides, S. A. Maier and R. F. Haglund, *Nano Lett.*, 2012, **12**, 780-786.
33. H. Guo, K. Chen, Y. Oh, K. Wang, C. Dejoie, S. A. Syed Asif, O. L. Warren, Z. W. Shan, J. Wu and A. M. Minor, *Nano Lett.*, 2011, **11**, 3207-3213.
34. L. Dai, C. X. Cao, Y. F. Gao and H. J. Luo, *Sol. Energy Mater. Sol. Cells*, 2011, **95**, 712-715.
35. M. Li, X. Wu, L. Li, Y. X. Wang, D. B. Li, J. Pan, S. J. Li, L. T. Sun and G. H. Li, *J. Mater. Chem. A*, 2014, **2**, 4520.
36. M. H. Lee and M. G. Kim, *Thin Solid Films*, 1996, **286**, 219-222.
37. Y. F. Sun, S. S. Jiang, W. T. Bi, R. Long, X. G. Tan, C. Z. Wu, S. Q. Wei and Y. Xie, *Nanoscale*, 2011, **3**, 4394-4401.
38. Y. J. Zhou, A. B. Huang, Y. M. Li, S. D. Ji, Y. F. Gao and P. Jin, *Nanoscale*, 2013, **5**, 9208-9213.
39. M. Maaza, O. Nemraoul, C. Sella and A. C. Beye, *Gold Bull.*, 2005, **38**, 100-106.
40. N. R. Mlyuka, G. A. Niklasson and C. G. Granqvist, *Sol. Energy Mater. Sol. Cells*, 2009, **93**, 1685-1687.
41. Z. T. Zhang, Y. F. Gao, Z. Chen, J. Du, C. X. Cao, L. T. Kang and H. J. Luo, *Langmuir*, 2010, **26**, 10738-10744.
42. L. T. Kang, Y. F. Gao, H. J. Luo, Z. Chen, J. Du and Z. T. Zhang, *ACS Appl. Mater. Interfaces*, 2011, **3**, 135-138.
43. N. R. Mlyuka, G. A. Niklasson and C. G. Granqvist, *Phys. Status Solid A,* 2009, **206**, 2155-2160.
44. Z. Chen, Y. F. Gao, L. T. Kang, J. Du, Z. T. Zhang, H. J. Luo, H. Y. Miao and G. Q. Tan, *Sol. Energy Mater. Sol. Cells*, 2011, **95**, 2677-2684.